Attributing uncertainties in simulated biospheric carbon fluxes to different error sources

J. C. Lin,[1] M. R. Pejam,[1,2] E. Chan,[1] S. C. Wofsy,[3] E. W. Gottlieb,[3] H. A. Margolis,[4] and J. H. McCaughey[5]

[1] Estimating the current sources and sinks of carbon and projecting future levels of CO_2 and climate require biospheric carbon models that cover the landscape. Such models inevitably suffer from deficiencies and uncertainties. This paper addresses how to quantify errors in modeled carbon fluxes and then trace them to specific input variables. To date, few studies have examined uncertainties in biospheric models in a quantitative fashion that are relevant to landscape-scale simulations. In this paper, we introduce a general framework to quantify errors in biospheric carbon models that "unmix" the contributions to the total uncertainty in simulated carbon fluxes and attribute the error to different variables. To illustrate this framework we apply and use a simple biospheric model, the Vegetation Photosynthesis and Respiration Model (VPRM), in boreal forests of central Canada, using eddy covariance flux measurement data from two main sites of the Canadian Carbon Program (CCP). We explicitly distinguish between systematic errors ("biases") and random errors and focus on the impact of errors present in biospheric parameters as well as driver data sets (satellite indices, temperature, solar radiation, and land cover). Biases in downward shortwave radiation accumulated to the most significant amount out of the driver data sets and accounted for a significant percentage of the annually summed carbon uptake. However, the largest cumulative errors were shown to stem from biospheric parameters controlling the light-use efficiency and respiration-temperature relationships. This work represents a step toward a carbon model-data fusion system because in such systems the outcome is determined as much by uncertainties as by the measurements themselves.

1. Introduction

[2] Since the beginning of the Industrial Revolution, concentrations of carbon dioxide (CO_2) in the atmosphere have increased by about 30% [*Keeling and Whorf*, 1994; *Crutzen and Stoermer*, 2000]. CO_2 is a key greenhouse gas, and changes in its biosphere-atmosphere fluxes under climate change play an important role in controlling future greenhouse concentrations and providing feedbacks to the climate system [*Friedlingstein et al.*, 2006; *Dufresne et al.*, 2002].

[3] Understanding biosphere-atmosphere exchanges of CO_2 is essential for predicting future climate trends. Terrestrial ecosystems absorb large amounts of atmospheric carbon dioxide through photosynthesis and release it through respiration and other microbiological processes. Using models to simulate and scale-up biosphere-atmosphere carbon exchanges is necessary when predicting carbon exchange over large regions and when projecting carbon fluxes into the future. Therefore, it is critical to examine the strengths and weaknesses associated with these models. This is particularly important in light of results from model intercomparison studies [*Amthor et al.*, 2001; *Kicklighter et al.*, 1999], which showed considerable differences in predicted carbon exchange by a variety of biospheric models. For instance, *Kicklighter et al.* [1999] compared global carbon biospheric models in which significant divergences in model simulations were found for summer uptake in boreal forests and during dry seasons of tropical evergreen forests.

[4] Although model intercomparison studies broadly identify the times and locations of divergences between different models, intercomparisons alone cannot provide quantitative assessment of model uncertainties. Determining uncertainties

[1]Department of Earth and Environmental Sciences, University of Waterloo, Waterloo, Ontario, Canada.
[2]Now at Climate Research Division, Environment Canada, Toronto, Ontario, Canada.
[3]Department of Earth and Planetary Science, Harvard University, Cambridge, Massachusetts, USA.
[4]Centre d'Études de la Forêt, Faculté de Foresterie, de Géographie et de Géomatique, Université Laval, Québec, Quebec, Canada.
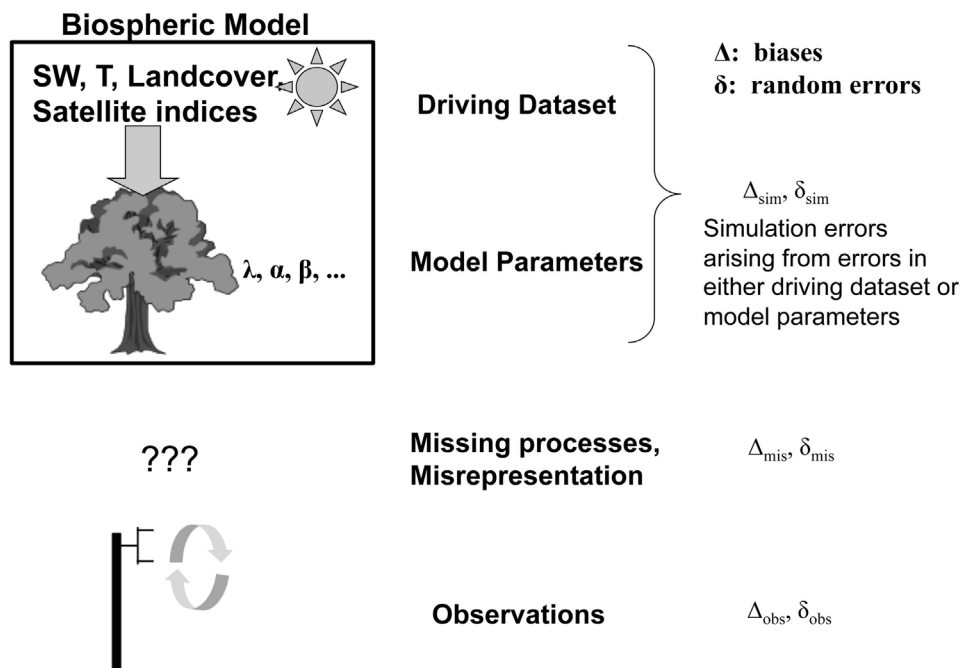[5]Department of Geography, Queen's University, Kingston, Ontario, Canada.

Figure 1. Schematic diagram of error analysis framework.

requires a more detailed look within individual models. While numerous modeling studies have included uncertainty considerations, few studies have systematically quantified the uncertainties in biospheric models in a way that is relevant for landscape-scale carbon studies. The shortcomings of previous analyses include.

[5] 1. Lack of single framework that considers all error sources: Previous uncertainty analyses have frequently entailed simple sensitivity analyses in which values of a small number of parameters or model formulations have been altered to observe their respective impacts [e.g., *Schaefer et al.*, 2008; *Kucharik et al.*, 2006]. While this is an important first step, there is an urgent need for a single analysis framework that attempts to consider all of the errors in a comprehensive manner. We attempt to do exactly this in the current paper, dividing the total error into contributions from various factors (Figure 1).

[6] 2. Lack of consideration for errors in driving environmental variables: Key environmental drivers such as temperature and solar radiation are often treated as perfectly known, or otherwise taken from observed values [*Zhou et al.*, 2008; *Sacks et al.*, 2006; *Davi et al.*, 2005]. Such observations are not available over the entire landscape, so when upscaling biospheric simulations, modeled values with their attendant errors need to be considered.

[7] 3. Neglecting errors in applying site-level parameters at larger scales: This issue is related to the classical problem of scaling in ecology [*Schulze et al.*, 1994; *Ehleringer and Field*, 1993]. Since observations of numerous parameters are available only at intensive research sites, parameter values are not known when the model is applied at other sites in spatial scaling applications. Numerous recent biospheric models rely heavily on site-level data, however. Examples include *Williams et al.* [1998], *Amthor et al.* [2001], *Grant et al.* [2006], and *Sun et al.* [2008]. Consequently, biospheric

models have been evaluated mostly at the site level, disregarding uncertainties involved in upscaling [*Williams et al.*, 2009]. Thus there is a need to either explicitly incorporate uncertainties in such parameters or use simple models that include less parameters.

[8] 4. Lack of distinction between random and systematic errors (biases): Random and systematic errors behave and influence results very differently, with systematic errors biasing estimates from model-data fusion systems while random errors simply increasing the posterior uncertainties [*Williams et al.*, 2009]. Although the impact of random versus systematic error differs, modeling studies have mostly considered only errors that are random [e.g., *Sacks et al.*, 2006; *Davi et al.*, 2005].

[9] The purposes of this paper are twofold. First, in response to the previously mentioned lack of relevant uncertainty studies, we introduce a general framework (Figure 1) to quantify errors in simulating biospheric carbon fluxes over the landscape. The framework methodically "unmixes" contributions to the total uncertainty in simulated carbon and attributes the total error to different factors. We apportion the total observed error into contributions from (1) driving data sets; (2) model parameters; (3) observations; and (4) model misrepresentation.

[10] Second, we show a specific application of the error analysis framework in the boreal forest region of central Canada, using eddy covariance flux measurement data from two main sites of the Canadian Carbon Program (CCP). We explicitly distinguish between systematic errors (i.e., "biases") and random errors. Special emphasis is placed upon examining the impact of biases, since over longer, annual time scales over which uptake and release cancel to a great extent to determine the net flux, biases are the errors that accumulate. However, random errors still act at subdaily time scales and would be relevant for quantifying deviations between models

and observations for "model-data fusion" purposes (see paragraph below).

[11] The specific biospheric model used as illustration of the error analysis framework is the Vegetation Photosynthesis and Respiration Model (VPRM) [*Mahadevan et al.*, 2008], a simple, data-driven diagnostic biosphere carbon flux model. VPRM has a simple mathematical structure with a minimum number of parameters. However, it has been shown that VPRM explains a significant percentage of observed variability (60–80% of hourly variability) at numerous sites, even given its simplicity [*Mahadevan et al.*, 2008]. This simplicity is important and enables partial derivatives that represent sensitivities of simulated carbon fluxes to various variables to be formulated easily.

[12] This study is envisioned as a step toward a "model-data fusion" approach to deriving carbon fluxes [*Raupach et al.*, 2005; *Williams et al.*, 2009]. A model-data fusion approach, also known as "data assimilation", makes corrections to models based on available observations. In this way, it attempts to calculate optimal estimates and provides estimates even when measurements are unavailable, in effect interpolating between observations in both space and time. As part of model-data fusion, prior estimates of errors play an important role, since they define the amount of anticipated deviance between observations and models [*Rodgers*, 2000]. It has been shown that inaccurate error estimates result in biased, erroneous estimates [*Raupach et al.*, 2005]. The framework discussed in this paper provides the error estimates in a quantitative fashion that can be used in model-data fusion systems.

2. Vegetation Photosynthesis and Respiration Model

[13] The Vegetation Photosynthesis and Respiration Model (VPRM) [*Mahadevan et al.*, 2008] is a diagnostic biospheric carbon flux model driven by satellite data, which provides independent information on the spatial and phenological variations of gross primary production using the Enhanced Vegetation Index (*EVI*) and Land Surface Water Index (*LSWI*), both from MODIS-Terra.

[14] VPRM calculates the net exchange of CO_2 between the atmosphere and the terrestrial biosphere ("Net Ecosystem Exchange"; *NEE*) for 12 main vegetation classes in each grid square separately, then scaled by vegetation fraction. Below, we introduce the governing equations in VPRM (section 2.1), the environmental driver data (section 2.2), the MODIS satellite indices (section 2.3), and then the land cover data (section 2.4).

2.1. VPRM Model Equations

[15] The Net Ecosystem Exchange (*NEE*) is the net difference between the photosynthetic uptake (*GEE*; "gross ecosystem exchange") and respiration (*R*) terms:

$$NEE = -GEE + R \qquad (1)$$

following the sign convention that uptake of CO_2 by plants is a negative flux (removal) from an atmospheric perspective.

[16] Following *Mahadevan et al.* [2008], *GEE* is modeled as a product between the light-use efficiency (*LUE*), the photosynthetically active radiation (*PAR*), and the fraction of *PAR* absorbed by the photosynthetically active foliage in the canopy (*FAPAR*):

$$GEE = LUE \times FAPAR \times \frac{1}{(1 + PAR/PAR_0)} \times PAR \qquad (2)$$

where PAR_0 is the half-saturation value. *PAR* in this study is derived from shortwave radiation (*SW*) using a conversion factor ϕ (see section 2.2):

$$PAR = \phi \cdot SW \qquad (3)$$

Xiao et al. [2004] have shown that the satellite-derived index *EVI* serves as a good proxy for *FAPAR*. In essence, *EVI* measures the "greenness" of the terrestrial biosphere and serves as a proxy for the amount of photosynthetically active foliage in the canopy. Following equation (9) in the work of *Mahadevan et al.* [2008], *GEE* is modeled as:

$$GEE = LUE \times EVI \times \frac{1}{(1 + PAR/PAR_0)} \times PAR \qquad (4a)$$

$$\text{where } LUE = \lambda \times T_{scale} \times P_{scale} \times W_{scale} \qquad (4b)$$

λ is the maximum *LUE* (a.k.a. quantum yield). T_{scale}, P_{scale}, and W_{scale} vary between 0 and 1.0 and represent the effect of temperature, leaf phenology, and canopy water content, respectively, on *LUE* by the photosynthetic mechanism. See *Mahadevan et al.* [2008] for details regarding T_{scale}.

[17] *LSWI* is used as an indicator of phenology and canopy water content:

$$P_{scale} = \frac{1 + LSWI}{2} \qquad (5)$$

$$W_{scale} = \frac{1 + LSWI}{1 + LSWI_{\max}} \qquad (6)$$

where $LSWI_{\max}$ is the maximum *LSWI* within the growing season for each pixel.

[18] Ecosystem respiration *R* is a simple linear function of temperature *T*:

$$R = \alpha \times T + \beta \qquad (7)$$

To capture the continued small amount of soil respiration during the winter, *T* is set to T_{low} when $T \leq T_{low}$. T_{low} is the soil temperature that is decoupled from the much colder air temperature in the presence of snow cover.

[19] The VPRM parameters and their values adopted in this study are summarized by *Mahadevan et al.* [2008, Table 2]. These values have been derived by fitting the model equations against eddy covariance data at sites associated with different land cover types (e.g., Harvard Forest for deciduous forest, Howland Forest for mixed deciduous/coniferous forest, and NOBS for evergreen boreal forest). Note that the two sites presented in this study for quantifying model uncertainties are not the same ones used originally for fitting parameters, thereby preserving the independence of model-data comparisons.

[20] The VPRM simulations are carried out at grids of 1/4° longitude by 1/6° latitude. However, subgrid-scale

contributions from different vegetation types are preserved, as the grid-scale *NEE* is simulated by weighing contributions from different vegetation types (f_k):

$$NEE = \sum_k f_k NEE_k \qquad (8)$$

where f_k is the fractional areal coverage by vegetation type k. f_k is derived from 1 km resolution vegetation data described in section 2.4.

2.2. NLDAS Radiation and Temperature

[21] To run VPRM, radiation and temperature data need to be combined with vegetation and water indices to calculate carbon fluxes. Hourly temperature (T) and incident shortwave radiation (SW) data have been retrieved from the North American Land Data Assimilation System (NLDAS) [*Cosgrove et al.*, 2003; *Mitchell et al.*, 2004]. The NLDAS-derived SW and T were downloaded in grid cells of 0.125° and then aggregated to grid cells of 1/4° longitude by 1/6° latitude.

[22] SW from NLDAS (in [W/m^2]) was converted to *PAR* (in [μmole photons/m^2/s]), since the rate of photosynthesis depends upon the rate of absorption of photons [*Nobel*, 1999]. We adopted a conversion factor (ϕ) of 1.98 between SW and *PAR*, following *Mahadevan et al.* [2008]. This is typical of ecosystem models, and the value of 1.98 falls within the range used by different ecosystem models [*Amthor et al.*, 2001]. An independent assessment of ϕ by regressing measured *PAR* against SW confirmed that the assumed value was close to the observed, with values of 1.96 and 1.98 at the Québec and Ontario sites (see section 5), respectively.

2.3. MODIS-Derived EVI and LSWI

[23] Multiyear satellite images from the MODIS sensor aboard the Terra satellite are processed to be used in VPRM. MODIS views the entire surface of the Earth every 1–2 days, measuring 36 spectral bands at 250 or 500 m resolution between 0.405 and 14.385 μm [*Mahadevan et al.*, 2008]. Eight day composite MODIS surface reflectances have been acquired to calculate the corresponding EVI and LSWI indices, which are then smoothed and linearly interpolated down to daily values [*Mahadevan et al.*, 2008].

2.4. Land Cover Data

[24] Following the application of VPRM over northeastern U.S. and southern Québec by *Matross et al.* [2006], we adopt the 1 km resolution Global Land Cover Characterization (GLCC) 2.0 land cover product [*Loveland et al.*, 2000]. The GLCC 2.0 data are then binned into 11 classes (10 vegetation + 1 water body). The 10 vegetation classes include: grassland, cropland, savanna, shrubland, mixed forest, deciduous forest, subtropical evergreen, dry temperate evergreen, wet temperate evergreen, and boreal evergreen [*Matross et al.*, 2006]. The 1 km resolution data are summed to yield f_k, the fractional areal coverage by vegetation type k in grid cells of 1/4° longitude by 1/6 ° latitude (equation (8)).

3. Error Analysis Framework

[25] Here we introduce the analysis framework that quantifies and attributes errors. Note that most of the following discussion is general and applies to all biospheric models, except for the part where variables specific to VPRM are considered.

[26] First, we consider that the simulated carbon flux F_{sim} deviates from the true flux F_{true} by an error ε:

$$F_{true} = F_{sim} - \varepsilon \qquad (9)$$

The negative sign is adopted in front of ε in order to preserve the commonly used definition of systematic errors and biases referring to (simulated – true) rather than (true – simulated). Note that ε can derive from both measurement (e.g., instrument errors) or model sources.

[27] If time is discretized into bins, the index i can be used to indicate a specific time bin:

$$F_{true,i} = F_{sim,i} - \varepsilon_i \qquad (10)$$

We adopted a time bin of 3 h in this study since autocorrelation of errors in simulated *NEE* was $> (1/e)$ at time scales within 3 h, suggesting that error characteristics within a 3-hourly time bin can be considered together as an unit when examining diurnal patterns in uncertainties.

[28] We explicitly distinguish between systematic errors (biases; Δ_i) versus random errors (δ_i), together which comprise ε_i:

$$\varepsilon_i = \Delta_i + \delta_i \qquad (11)$$

Following Figure 1, we partition the bias and random error into (1) the contribution caused by processes that are already incorporated into the model (*sim*); (2) that due to missing processes or misrepresentation in the model structure (*mis*); and (3) the error in the observations (*obs*):

$$\varepsilon_i = \varepsilon_{sim,i} + \varepsilon_{mis,i} + \varepsilon_{obs,i} = \Delta_{sim,i} + \delta_{sim,i} + \Delta_{mis,i} + \delta_{mis,i}$$
$$+ \Delta_{obs,i} + \delta_{obs,i} \qquad (12)$$

Broadly speaking, ε_{sim} represents uncertainties that result from erroneous values for drivers and model parameters. ε_{mis}, on the other hand, refers to the residual uncertainty that would be present even if "perfect" drivers or model parameters are adopted.

[29] Examples of $\Delta_{sim,i}$ and $\Delta_{mis,i}$ are as follows. The respiration term in VPRM is currently modeled as a linear function of T for $T > T_{low}$. If the simulated T from atmospheric gridded data sets is systematically lower than observed, this would cause a negative $\Delta_{sim,i}$. However, systematic errors would also arise if the respiration exhibits exponential dependence on T. The deviation from linear behavior would then be considered a part of $\Delta_{mis,i}$.

[30] Combining equations (10) and (12):

$$F_{true,i} = F_{sim,i} - \Delta_{sim,i} - \Delta_{mis,i} - \Delta_{obs,i} - \delta_{sim,i} - \delta_{mis,i} - \delta_{obs,i}$$
$$(13)$$

The systematic error is defined to be a constant offset persisting over a particular period of time. When averaged over

this time period, indicated by the overbar, the random errors go to 0, leaving the bias terms:

$$\overline{F_{true,i}} = \overline{F_{sim,i}} - \overline{\Delta_{sim,i}} - \overline{\Delta_{mis,i}} - \overline{\Delta_{obs,i}} - \overline{\delta_{sim,i}} - \overline{\delta_{mis,i}} - \overline{\delta_{obs,i}}$$

$$\overline{F_{true,i}} = \overline{F_{sim,i}} - \Delta_{sim,i} - \Delta_{mis,i} - \Delta_{obs,i} - 0 - 0 - 0$$

$$\overline{F_{sim,i}} - \overline{F_{true,i}} = \Delta_{sim,i} + \Delta_{mis,i} + \Delta_{obs,i} \qquad (14)$$

We chose an averaging period of 1 month. Thus Δ represents the bias terms during a 3-hourly bin i, over a month. For brevity's sake the index i is dropped in subsequent equations.

3.1. Attributing Random Errors to Different Variables

[31] The simulated biospheric flux F_{sim} is a function of various environmental drivers and model parameters (x_j): $F_{sim} = f(x_1, x_2, x_3, \cdots x_j)$. Under a first-order approximation, the simulation error is given by [*Taylor*, 1997]:

$$\varepsilon_{sim} \approx \sum_j \frac{\partial F_{sim}}{\partial x_j} \varepsilon_{x_j} \text{ where } \varepsilon_{x_j} = (x_{j,sim} - x_{j,true}) \qquad (15)$$

The partial derivative represents the "sensitivity" of simulated flux F_{sim} to variable x_j. When arranged in matrix format, the partial derivatives comprise elements of the Jacobian matrix.

[32] In the case of VPRM, F_{sim} is a function of the following variables, broadly divided into drivers and model parameters:

$$F_{sim} = f\left(\underbrace{EVI, LSWI, land, T, SW}_{drivers}, \underbrace{\lambda, \alpha, \beta, \phi, PAR_0 \cdots}_{parameters} \right) \qquad (16)$$

where *land* refers to the fractional land cover f_k of different vegetation types k.

[33] The random simulation error is a sum of the individual contributions from the various drivers and parameters:

$$\sigma_{sim}^2 = \sigma_{EVI}^2 + \sigma_{LSWI}^2 + \sigma_{land}^2 + \sigma_T^2 + \sigma_{SW}^2 + \cdots \qquad (17)$$

The contribution from each variable is estimated as follows:

$$\sigma_{EVI} = \sigma\left(\frac{\partial F_{sim}}{\partial EVI} [EVI_{sim} - EVI_{true}] \right);$$

$$\sigma_{LSWI} = \sigma\left(\frac{\partial F_{sim}}{\partial LSWI} [LSWI_{sim} - LSWI_{true}] \right); \cdots \qquad (18)$$

where $\sigma(\cdots)$ refers to the standard deviation function. $\sigma(land) = 0$, since the error in vegetation cover persists throughout the simulation and should thus be considered as a bias term.

[34] Due to simplicity of the VPRM's governing equations the partial derivatives can be analytically derived with ease. For instance, starting from equation (4) and taking the partial derivative with respect to *PAR*:

$$\frac{\partial F_{sim}}{\partial PAR} = \frac{-\partial GEE_{sim}}{\partial PAR} = \frac{-1}{\phi} \frac{\partial GEE_{sim}}{\partial SW}$$

$$= -\lambda \times T_{scale} \times P_{scale} \times W_{scale} \times EVI$$

$$\times \left[\frac{1}{(1 + PAR/PAR_0)} - \frac{PAR}{PAR_0(1 + PAR/PAR_0)^2} \right] \qquad (19)$$

In the case of more complicated models the partial derivatives can be calculated with numerical simulations. In the case above, *PAR* would be first perturbed to see the effect on F_{sim}.

[35] Since errors in variables like T and *land* can affect both *GEE* and *R*, we explicitly distinguished the random errors in $-GEE$ versus R:

$$\sigma_{sim}^2 = \sigma_{EVI,-GEE}^2 + \sigma_{LSWI,-GEE}^2 + \sigma_{land,-GEE}^2 + \sigma_{land,R}^2$$

$$+ \sigma_{T,-GEE}^2 + \sigma_{T,R}^2 + \sigma_{SW,-GEE}^2 + \sigma_{SW,R}^2 + \cdots \qquad (20)$$

$-GEE$ rather than GEE is adopted here in order to keep the same sign convention as F_{sim}: e.g., an overestimation of SW would result in F_{sim} being more negative (more removal from the atmosphere).

3.2. Attributing Biases to Different Variables

[36] To determine the contribution to the simulation error from biases, equation (15) is time averaged $\overline{(\cdots)}$:

$$\overline{\varepsilon_{sim}} = \Delta_{sim} \approx \sum_j \overline{\frac{\partial F_{sim}}{\partial x_j} \varepsilon_{x_j}} \quad \text{where } \varepsilon_{x_j} = (x_{j,sim} - x_{j,true}) \quad (21)$$

Similar to equations (17) and (20), the total simulation bias Δ_{sim} can be partitioned into contributions from different variables:

$$\Delta_{sim} = \Delta_{EVI} + \Delta_{LSWI} + \Delta_{land} + \Delta_T + \Delta_{SW} + \Delta_{LUE} + \Delta_{PAR_0} + \cdots$$

$$\Delta_{sim} = \Delta_{EVI,-GEE} + \Delta_{LSWI,-GEE} + \Delta_{land,-GEE} + \Delta_{land,R}$$

$$+ \Delta_{T,-GEE} + \Delta_{T,R} + \Delta_{SW,-GEE} + \Delta_{LUE,-GEE}$$

$$+ \Delta_{PAR_0,-GEE} + \cdots \qquad (22)$$

The terms found on the RHS of equation (22) are the ones specifically considered in this study. We consider the effect of biases in *LUE* rather than attempting to further distinguish errors in its subcomponents in equation (4b) (λ, T_{scale}, P_{scale}, and W_{scale}).

[37] To determine each of the terms in equation (22), the time-averaging operator is applied to the product between the partial derivative and the error in a particular variable. For instance, Δ_T is given by:

$$\Delta_T = \overline{\frac{\partial F_{sim}}{\partial T} (T_{sim} - T_{true})} = \overline{\frac{\partial(-GEE + R)}{\partial T} (T_{sim} - T_{true})}$$

$$= \overline{\frac{\partial(-GEE)}{\partial T} (T_{sim} - T_{true})} + \overline{\frac{\partial R}{\partial T} (T_{sim} - T_{true})}$$

$$\Delta_T = \underbrace{\overline{\frac{\partial(-GEE)}{\partial T} (T_{sim} - T_{true})}}_{\Delta_{T,-GEE}} + \underbrace{\overline{\alpha(T_{sim} - T_{true})}}_{\Delta_{T,R}} \qquad (23)$$

Because x_{true} is not known, we approximated $\varepsilon_{x_j} = (x_{j,sim} - x_{j,true})$ with the difference between simulated and observed values:

$$\varepsilon_{x_j} \approx (x_{j,sim} - x_{j,obs}) \qquad (24)$$

Where possible we attempted to account for the measurement error:

$$\sigma^2(x_{j,sim} - x_{true}) = \sigma^2(x_{j,sim} - x_{j,obs}) - \sigma^2(x_{j,obs} - x_{j,true}) \qquad (25)$$

Measurement errors were considered for eddy covariance data (section 4.1). For T and SW, however, we did not include such error estimates, with the assumption that the simulation errors in these cases likely dominate the measurement errors. In any case, neglecting the measurement error provides an upper limit estimate of the random error.

4. Method for Estimating Errors in Different Variables

4.1. Errors in Eddy Covariance Measurements

[38] The eddy covariance method provides a direct measurement of the net exchange of fluxes between a vegetated surface and the atmosphere and has significant advantages in that it allows continuous data collection over a spatial region over hundreds of meters [*Baldocchi*, 2003].

[39] Random errors of eddy covariance measurements have been found to be a function of wind speed, decreasing linearly as wind speed increases [*Hollinger and Richardson*, 2005]. We follow this formulation and adopt the empirically derived relationship at a mixedwood forest in Maine, USA (growing season: $\sigma_{obs} = 3.76 - 0.43\overline{u}$; nongrowing season: $\sigma_{obs} = 0.86 - 0.056\overline{u}$) from *Hollinger and Richardson* [2005]. These authors also pointed out that the eddy covariance errors follow a double-exponential rather than a Gaussian distribution.

[40] Missing data at eddy covariance sites arise from data rejections or instrument malfunction [*Falge et al.*, 2001]. Due to the necessity to sum the eddy covariance data to obtain time-integrated fluxes over periods of months or years (section 6.6), the missing data have to be accounted for with gap-filling procedures. The procedure has been standardized within Fluxnet-Canada to enable intersite comparisons.

[41] The standard Fluxnet-Canada gap-filling protocol, explained in detail by *Barr et al.* [2004], separately accounts for gaps during daytime (photosynthesis + respiration) and nighttime (respiration), as the relevant controlling variables are different for photosynthesis and respiration. Gaps in respiration are filled using an empirical function of T using a logistic relationship; gaps in photosynthesis are accounted for with measured PAR using a hyperbolic equation. The *Barr et al.* [2004] methodology also uses a moving window approach, thus incorporating time-varying parameters in the empirical fits.

[42] We only used the directly measured (non-gap-filled) NEE to evaluate uncertainties in the simulations. The gap-filled values are used solely to assess errors in the cumulative carbon budget summed over monthly to annual time scales (section 6.6).

4.2. Errors in MODIS Satellite Indices

[43] Satellite measurement errors arise from sources such as "sensor noise, calibration drift, orbital decay, and incorrect geolocation" [*Raupch et al.*, 2005].

[44] For the MODIS surface reflectance-derived EVI and $LSWI$, noises would originate from contributing uncertainties in the MOD09 product such as aerosol optical thickness error, aerosol model error, and reflectance approximation error as well as calibration error [*Vermote and Vermeulen*, 1999; *Vermote and Saleous*, 2006]. Considering the final EVI values, 93.64% of globally retrieved EVI values fall within

the theoretical MODIS 1-sigma error bar, meaning that the error in a given index value is 0.02 plus 2% of the index value [*Vermote and Kotchenova*, 2008]. The $LSWI$ error should also conservatively fall within $\pm (0.02 + 0.02\ LSWI)$, given the similarities in its mathematical formulation with EVI and $NDVI$ as well as the theoretical calculation given by *Vermote and Kotchenova* [2008].

4.3. Errors in Land Cover Data

[45] We quantified errors in the GLCC 2.0 land cover product by comparing against the high-resolution Ontario Land Cover database (http://www.lib.uoguelph.ca/resources/data_resource_centre/geospatial_data_resources/ontario_provincial_land_cover_database.cfm). [*Ontario Ministry of Natural Resources*, 2002]. The Ontario Land Cover database is a high-quality land cover product derived from the LANDSAT Thematic Mapper satellite data (30m spatial resolution) using a supervised classification method, informed by field knowledge. The 28 classes are regrouped to the same 11 classes as was the GLCC and summed to yield the same fractional area occupied by each class within a 1/4° longitude by 1/6° latitude grid cell.

[46] In aggregate, the standard deviation of the difference between GLCC and the Ontario Land Cover database was 0.27, meaning that the GLCC deviated from the Ontario Land Cover database by 27% for a particular vegetation class, on average. The Ontario product itself possessed residual errors, with approximate 90% accuracy for forest classes (see http://www.lib.uoguelph.ca/resources/data_resource_centre/geospatial_data_resources/components/documents/landcover_readme.pdf), translating into a remaining error of 10%. Since the aggregate standard deviation of 27% includes errors in the Ontario product, error incurred by adopting the GLCC land cover database, then, is $\sqrt{0.27^2 - 0.10^2} = 0.25$, or 25%. Note that this is likely a conservative (over) estimate of the land cover error, since the 10% error in a small grid cell of 30 m would be decreased due to error cancellation once these are aggregated to $1/4° \times 1/6°$.

4.4. Errors in PAR_0, LUE

[47] The eddy covariance sites yield estimates of GEE by combining direct measurements of daytime NEE and a temperature function describing R [*Bergeron et al.*, 2007]. GEE estimates (all non-gap-filled) were regressed against observed PAR to determine "measured" PAR_0 and LUE, which were compared against the model's values of PAR_0 and LUE to quantify the model's errors in these biospheric parameters (section 6.3). However, these two parameters are difficult to determine separately from eddy covariance data: a large value for PAR_0 is compensated by a lower LUE, producing the same flux. Due to this strong negative correlation [*Hollinger and Richardson*, 2005], we carefully consider the confidence intervals and interpret the results accordingly.

[48] Specifically, the following steps were adopted to derive PAR_0 and LUE from eddy covariance measurements:

[49] 1. "Measured" PAR_0 was determined for each site by carrying out a nonlinear least-squared fit between eddy covariance-derived GEE and $PAR/(PAR + PAR_0)$ for the months of May–September.

[50] 2. The 95% confidence intervals of PAR_0 were extracted from the statistical fit in Step 1.
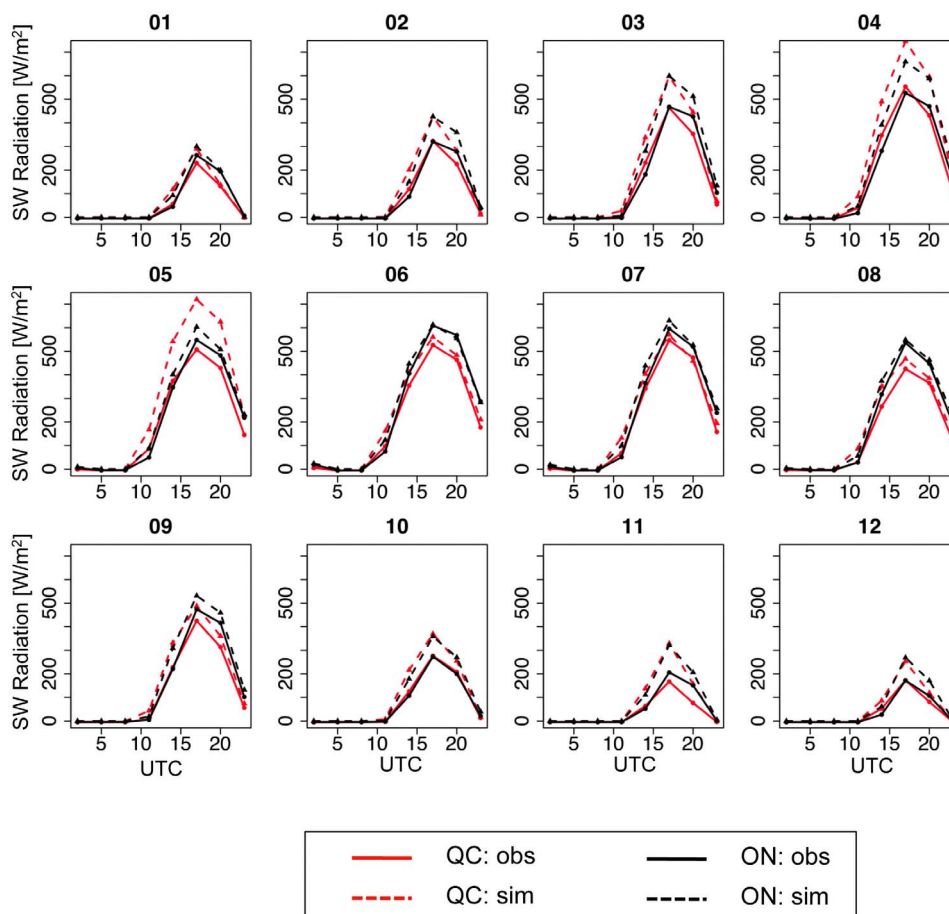
Figure 2. Average diurnal cycle of shortwave radiation (*SW*) at the Québec (QC; red) and Ontario (ON; black) study sites for all 12 months of 2004. Observed values are shown with solid lines, while the modeled data from NLDAS are indicated with dashed lines. Hour of day is in UTC.

[51] 3. Monthly values of "measured" *LUE* were calculated as the linear regression slope between *GEE* and [*EVI* × *PAR*/(1 + *PAR*/PAR_0)], following equation (4).

[52] 4. Due to the negative correlation between PAR_0 and *LUE* Step 3 was repeated for the upper and lower limits of the 95% confidence interval in PAR_0, to provide an indication of the ranges that these two parameters can take. The upper and lower ranges of PAR_0 and *LUE* will be carried through in subsequent analyses (sections 6.3 and 6.6.2).

5. Study Area and Flux Stations

[53] We illustrate the application of the error analysis framework in central Canada. Observations made in 2004 from two eddy covariance flux measurement sites in Ontario and Québec are used for the error analysis. These two stations are representative of central and eastern Canadian boreal forests and are core sites in the Canadian Carbon Program (CCP). The CCP and its predecessor, Fluxnet-Canada (FCRN), are composed of a national network of flux tower sites distributed across an east-west transect in Canada's southern boreal region. Over the past several years, CCP/ FCRN has made important contributions to knowledge of the Canadian carbon cycle [*Coursolle et al.*, 2006; *Margolis et al.*, 2006]. Canada plays a significant role in the global

carbon budget, since the Canadian landscape contains about 10% of the world's forests [*Kurz and Apps*, 1999].

5.1. Site Description: Québec Eastern Old Black Spruce ("QC")

[54] The Québec Eastern Old Black Spruce Forest site represents a dominant cover type in the boreal forests of North America [*Bergeron et al.*, 2007]. This site (49.692° N, 74.342° W) is located 30 km south of Chibougamau, Québec, and lies about halfway between the southern and northern (treeline) limits of the boreal forest. The flux footprint (90% isopleths in the along-wind direction) corresponds to an approximate 500 m radius centered on the tower and is mainly covered by black spruce (*Picea mariana* (Mill.) B.S.P.), with a small amount of jack pine (*Pinus banksiana*) and tamarack (*Larix laricina*). Most of the study area was burned between 1885 and 1915. For further details of site characteristics and instrumentations, see *Bergeron et al.* [2007].

5.2. Site Description: Ontario Mixedwood

[55] The old mixedwood site at the Ontario flux station (a.k.a. "Groundhog River Flux Station"), is representative of a mature mixedwood boreal forest. The site (48.217° N, 82.156° W) is a typical boreal mixedwood forest located approximately 80 km southwest of Timmins in northern
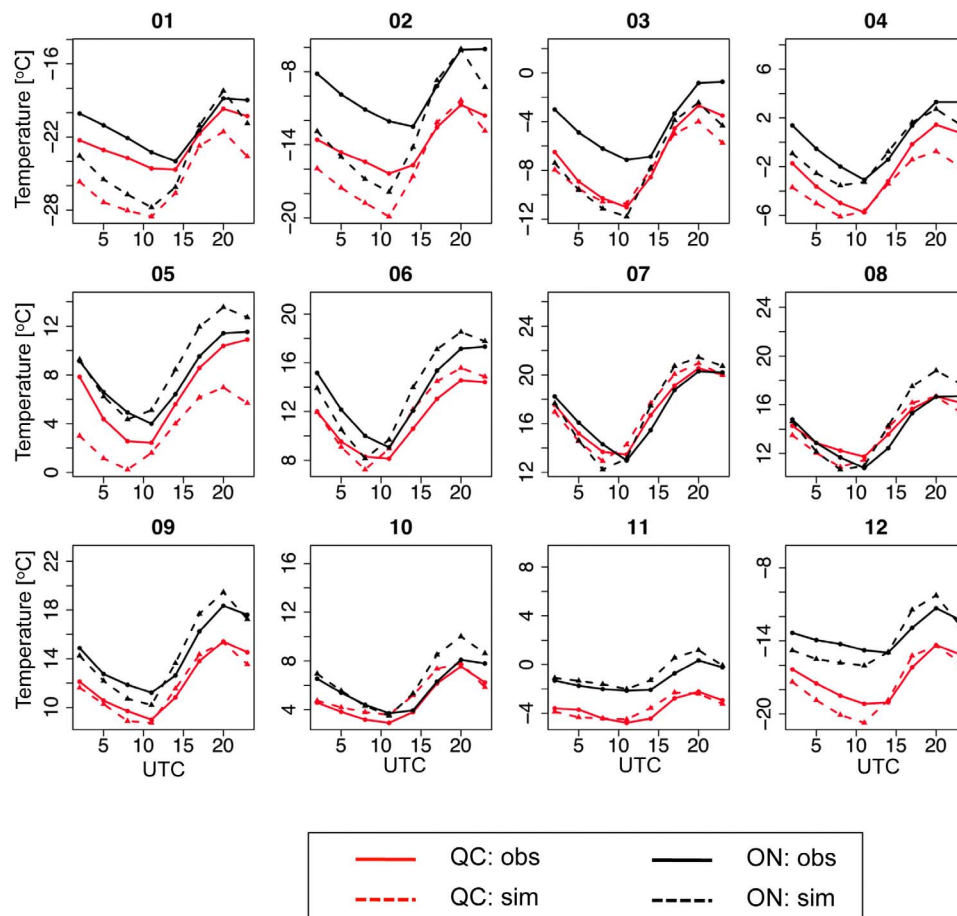
Figure 3. Average diurnal cycle of temperature (T) at the Québec (QC; red) and Ontario (ON; black) study sites. Similar to Figure 2.

Ontario. The forest regenerated after high-grade logging in the 1930s. For further details of instrumentation and site characteristics, see *McCaughey et al.* [2006] or *Pejam et al.* [2006].

[56] Hereafter we will refer to the Ontario and Québec sites as "ON" and "QC", respectively.

6. Results

6.1. Environmental Driver Comparisons

[57] In Figures 2–3, we compare the NLDAS-modeled environmental drivers (SW, T) versus the observed values as average diurnal cycles over the entire 12 months of 2004. At both QC and ON a systematic overestimation (sunny bias) is observed during the afternoon. The overestimation is especially pronounced during the spring and fall months: March–May and October–November in QC; March–April and October–November in ON.

[58] At ON, overestimation of T (warm bias) during the afternoon of the peak growing season of June–August is observed. A significantly larger cold bias is observed during the winter nighttime at both sites: January–February in QC and January–March in ON.

[59] The sunny bias in NLDAS can be traced to the GOES-based radiation product, particularly at low zenith

angles [*Mitchell et al.*, 2004]. The problem is exacerbated at angles below 75 degrees, when the GOES product is substituted with radiation in EDAS, which exhibits even larger biases [*Betts et al.*, 1997]. We currently do not know the source of the T bias in NLDAS.

[60] The implications of the aforementioned biases on simulated *NEE* will be explored in sections 6.2, 6.5, and 6.6.

6.2. NEE Comparisons

[61] Comparisons between simulated and observed hourly *NEE* over the entire year in 2004 yielded $R^2 = 0.58$ (ON) and $R^2 = 0.63$ (QC). The average diurnal *NEE* cycles are shown in Figure 4. In these plots, observed values are not plotted when > 50% of hourly observations are missing within a 3-hourly time bin in a given month.

[62] At both sites, the winter months (December, January, and February) are quiescent with regards to carbon dynamics, with a low level of carbon efflux persisting throughout those months. VPRM captures this low level of "background" carbon efflux, despite the observed cold bias, because respiration is simulated with T_{low} when $T \le T_{low}$, so the lower-than-observed T would not bias by itself the simulated wintertime respiration.

[63] During the summer months of June–August a pronounced diurnal cycle is observed, with nighttime release
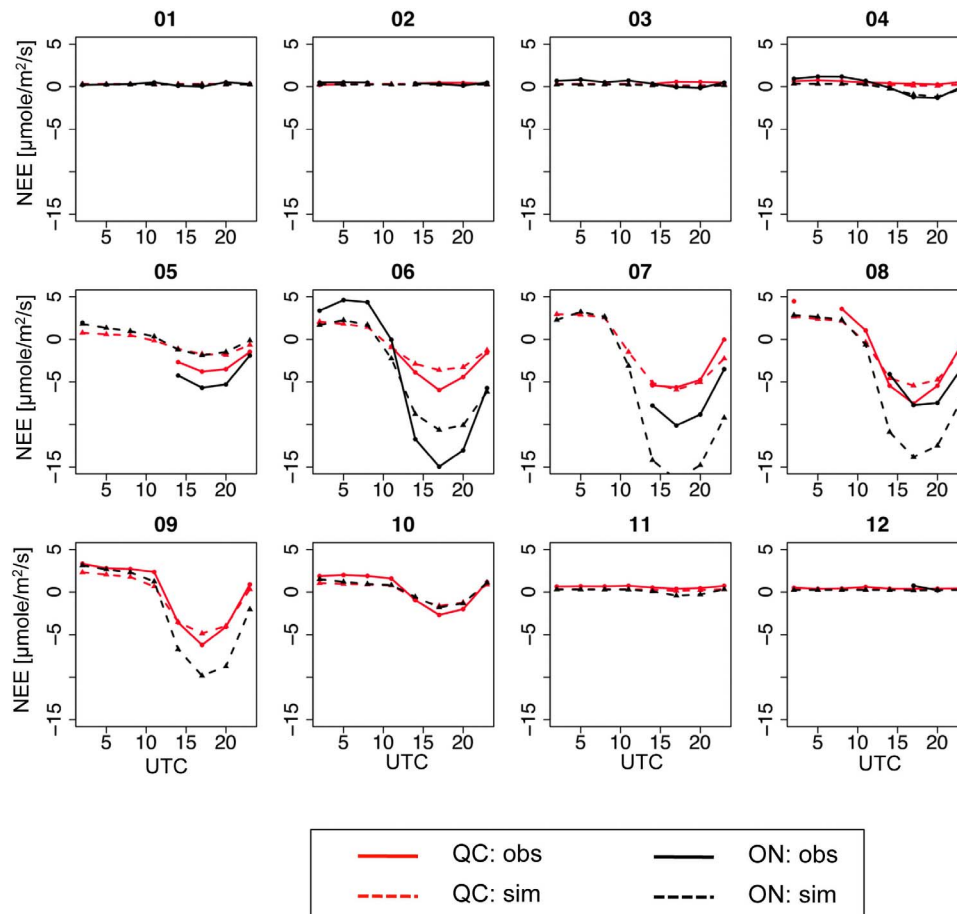
Figure 4. Average diurnal cycle of Net Ecosystem Exchange (*NEE*) of carbon at the Québec (QC; red) and Ontario (ON; black) study sites for all 12 months in 2004. Observed values are shown with solid lines, while simulated values from the VPRM biospheric model are indicated with dashed lines. The sign convention is such that negative values indicate net removal of carbon from the atmosphere by the biosphere, indicative of carbon uptake by photosynthesis. Observations are not plotted when >50% of hours within a 3-hourly time bin are missing.

and daytime uptake of CO_2. The diurnal amplitude is larger at ON. VPRM underestimates the afternoon uptake at ON in May–June but overestimates it in July–August. Such errors are much smaller at QC. In fact, the large afternoon sunny bias in May at QC did not translate into an excess of uptake. This was because the magnitude of $-\partial GEE / \partial SW$ was still small in May.

[64] During the next few sections, we will examine the factors contributing to the observed model-measurement deviances.

6.3. LUE and PAR₀ Comparisons

[65] Because VPRM is based on the light-use efficiency (*LUE*) paradigm (equation (4)), understanding errors in the relationship between *GEE* and light (*PAR*) is fundamental to evaluating errors in the model. This is carried out in two steps: by first evaluating PAR_0 and then the *LUE*.

[66] PAR_0 derived empirically from the eddy covariance data using a nonlinear fit (section 4.4) was compared against the value in VPRM. Since assumed PAR_0 differed between vegetation types, the model's value was calculated as a fractional coverage-weighted average between the assumed

values for different vegetation types. Values of PAR_0, in [μmole/m²/s], are as follows: 269 (obs) versus 431 (model) at QC; 420 (obs) versus 606 (model) at ON. The resulting curves, which include the confidence intervals for the non-linear fit, are shown in Figure 5. The higher PAR_0 assumed in the model resulted in greater *GEE* for a given *PAR* for both sites.

[67] Comparisons between measured *LUE* and simulated values are shown in Figure 6. At QC, the simulations underestimated *LUE* throughout the entire growing season. At ON, the underestimation of *LUE* was also present except when the drop in observed *LUE* during the months of July–September, resulted in a temporary overestimation.

[68] The importance of vapor pressure deficit (*VPD*) in diminishing *GEE*, particularly pronounced during the summer daytime, at the ON site has been pointed out by *McCaughey et al.* [2006]. We examined the potential impact of *VPD* by introducing another scalar ranging between 0 and 1.0 that lowers *LUE* with higher *VPD*. The parameterization follows the MODIS Land Algorithm [*Heinsch et al.*, 2003]: a linear ramp function that decreases from 1.0 to 0 between $VPD_{min} = 650$ Pa and $VPD_{max} = 2500$ Pa. These parameter
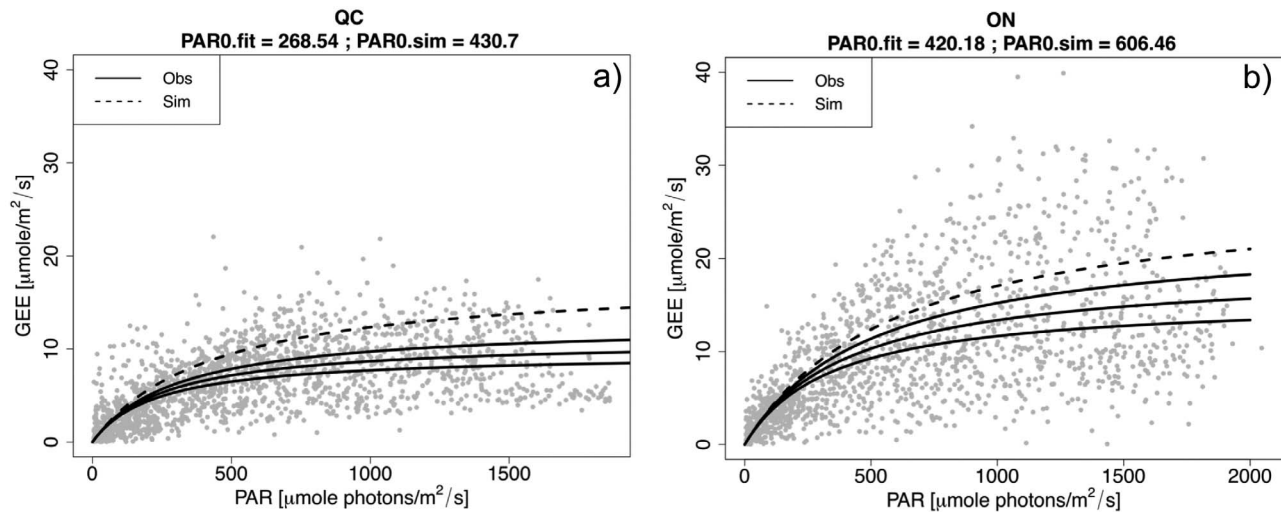
Figure 5. The observed *GEE* versus *PAR* relationship and the nonlinear fit to the data (solid lines), following equation (4), for (a) QC and (b) ON. The three solid lines indicate the fitted as well as the 95% confidence interval for the fitted relationship; QC: $236 \leq PAR_0 \leq 311$; ON: $348 \leq PAR_0 \leq 508$. The assumed relationship simulated by VPRM is shown as the dashed line.

values characterize evergreen needleleaf forest and mixed forest in the look-up table used by the same MODIS Land Algorithm [*Heinsch et al.*, 2003].

[69] At ON, including a *VPD* effect reduced the simulated *LUE* between the months of June–September. At QC, the seasonal pattern in simulated *LUE* exhibited closer resemblance to the observed pattern when *VPD* was accounted for, by especially lowering the July *LUE*. However, since the *VPD* effect serves only to lower *LUE*, it alone cannot explain the significant underestimation of *LUE* by the model.

[70] Because of the central role played by *LUE* in VPRM, systematic errors in *LUE* generally correspond to systematic differences in *NEE* (Figure 4): months when the model

underestimated daytime carbon uptake matched months when *LUE* was also underestimated, and vice versa. The underestimation of *LUE* was partly counteracted by the overestimation of PAR_0 (Figure 5). The accumulated impact of biases in PAR_0 and *LUE* on carbon fluxes over multimonth to annual time scales will be examined in section 6.6 and compared against the impact of other variables.

6.4. Comparisons of Respiration-Temperature Relationships

[71] The dependence of *R* on *T* was compared between the model and observations. The measured relationship was derived by fitting α, β, and T_{low} (section 2.1) against night-
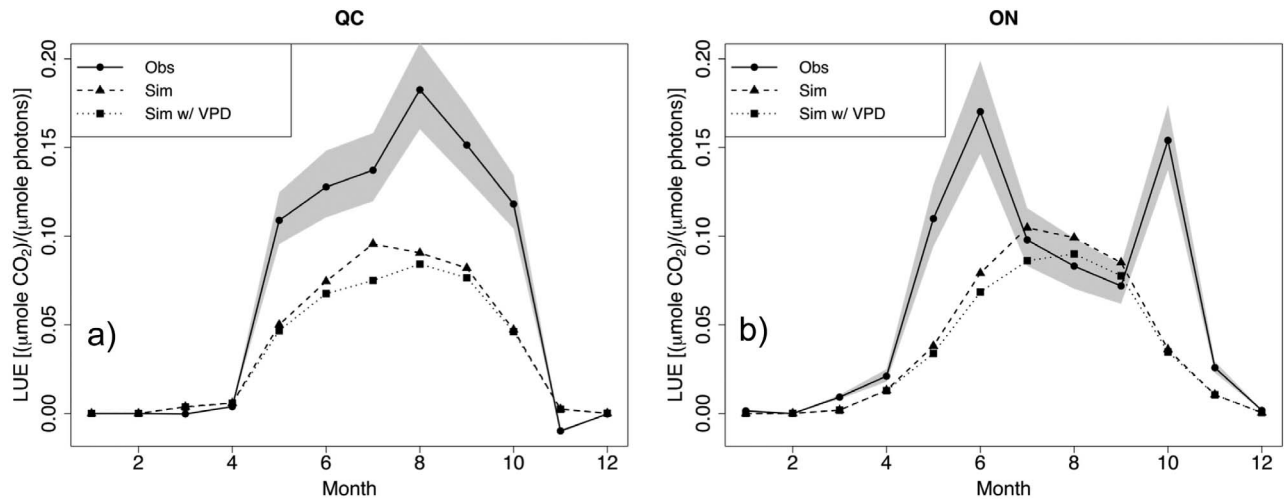

Figure 6. Comparison of monthly averaged light-use efficiency (*LUE*) between simulations (dashed line) and eddy covariance-derived values (solid line; section 4.4), at (a) QC and (b) ON. The simulations modified with *VPD* effect (dotted line) are also shown. The shaded region indicates the range of *LUE* values that results from the range in fitted PAR_0 (Figure 5): due to the negative correlation between "observed" PAR_0 and *LUE* fitted from eddy covariance fluxes, a PAR_0 in the upper range results in the lower range of *LUE*.
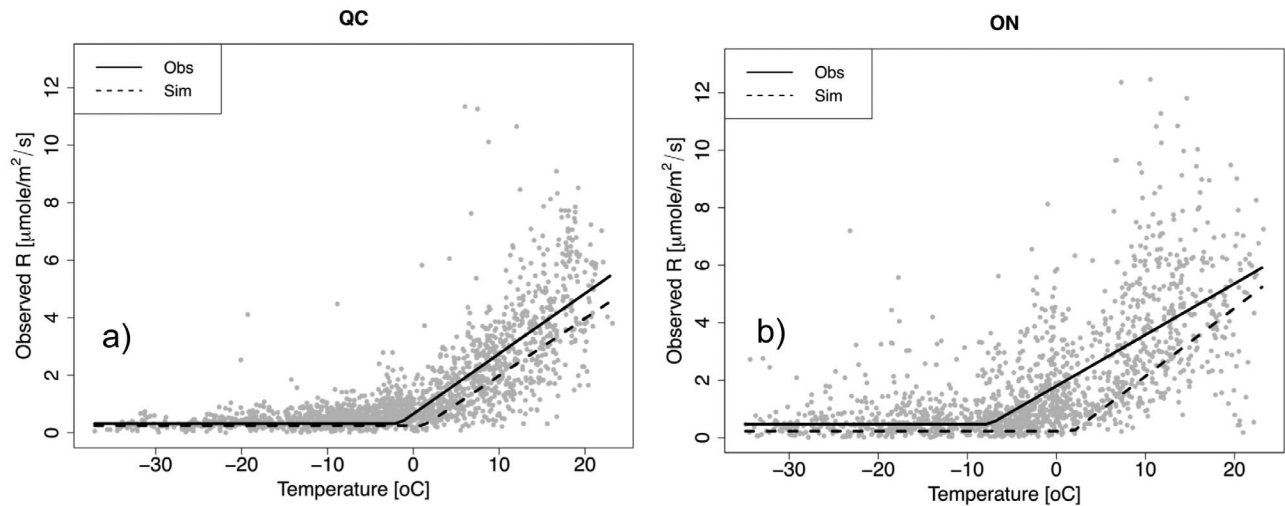
Figure 7. The T dependence of R at (a) QC and (b) ON. The nonlinear fit to the data is shown as the solid line, while the VPRM's assumed relationship is shown as the dashed line. Note that T is set to T_{low} when $T \leq T_{low}$, so during wintertime conditions R is a constant ($= \alpha \times T_{low} + \beta$).
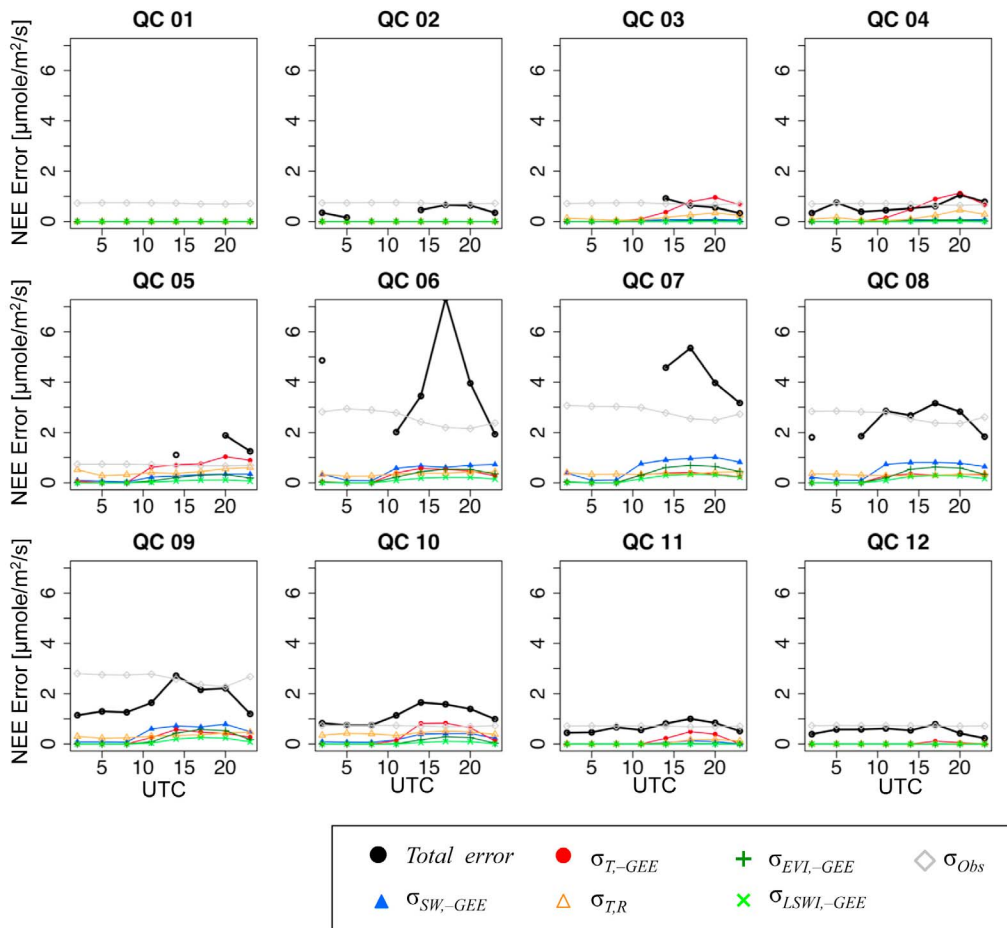

Figure 8. Random errors in *NEE* at QC in each 3-hourly bin over the diurnal cycle in all 12 months of 2004, and the contributions from different sources, following equations (15) and (18).
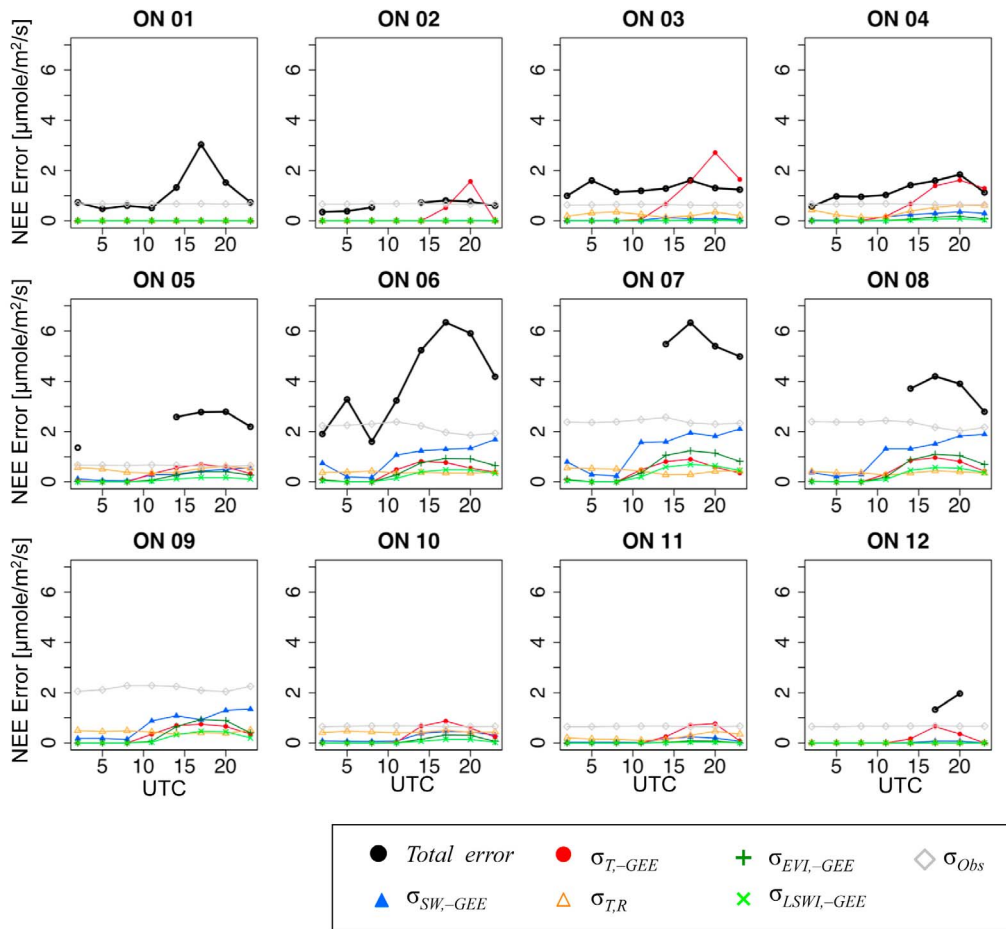
Figure 9. Random errors in *NEE* for the Ontario (ON) study site. Similar to Figure 8.

time *NEE* measurements. The data-derived relationship (solid) as well as the assumed VPRM relationship simulation (dashed) are shown in Figure 7.

[72] The relationship between *R* and *T* is noisy, particularly at ON. This has already been recognized by previous researchers [*Davidson et al.*, 2006].

[73] T_{low} can be seen as the value of *T* at which the line switches from a horizontal line (background *R* at low *T*) to a constant positive slope at higher *T*. The assumed values of T_{low} were higher than fitted values, with the difference being bigger at ON, where the low-level *R* and release of carbon persisted even at $T < -10°C$.

[74] The net result of the discrepancy in the *R-T* relationship is that *R* is underestimated in VPRM, as already witnessed in the nighttime simulated *NEE* being systematically smaller than measured (Figure 4). In section 6.6 we will see the implications of this departure on monthly to annual-scale carbon exchange.

6.5. Attributing Random Errors to Different Environmental Drivers

[75] Figures 8 and 9 show the random errors and the contributions by each driver variable at the hourly time scale. F_{obs} was the largest contributor to random errors in almost all months, suggesting that the discrepancy between the model and eddy covariance from hour to hour can be explained

to a great extent by scatter in the eddy covariance measurements. Additionally, *T* exhibits relatively large effects during the afternoons of March–May in QC and February–April in ON. During the growing season months, the contributions derive from diverse sources, with errors in *SW*, *T*, *EVI*, and *LSWI* all contributing.

6.6. Effects of Biases on Monthly and Annual Carbon Fluxes

[76] In this section, we examine how systematic errors (biases) accumulate at the monthly to annual time scales. The interest in monthly to annual carbon fluxes stems from the fact that due to the diurnal and seasonal sign reversals in carbon fluxes (Figure 4), the net carbon storage or release is a small net amount resulting from accumulating the fluxes, over monthly to annual time scales. Accordingly, the effects of biases need to be evaluated at such time scales. As shown in Figure 1, we separate out the impact of biases in environmental drivers (section 6.6.1) versus biases in model parameters (section 6.6.2).

6.6.1. Effects of Biases in Environmental Drivers

[77] Results at QC (Figure 10) indicate that monthly biases in modeled carbon due to *T* are small and accumulate to small values over a year. In contrast, the bias due to *SW* is almost identical to the total observed bias of −0.71 t C/ha. This suggests that the *SW* bias results in a significant effect
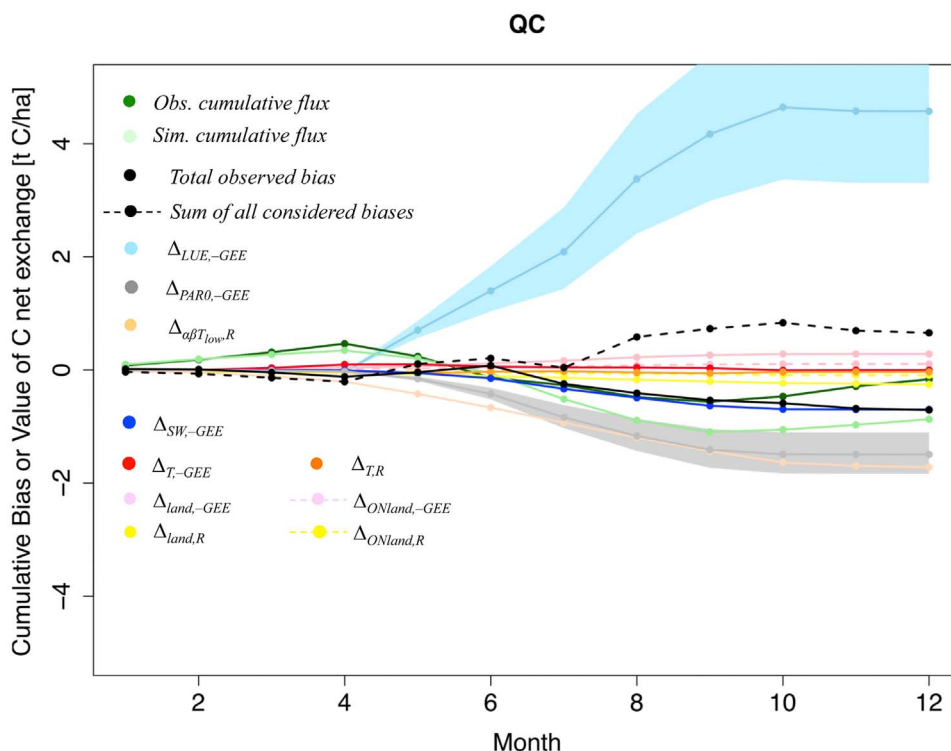
Figure 10. Cumulative biases in NEE ($F_{sim} - F_{obs}$) in 2004 at QC and the contributions from different error sources. The values indicated at the end of the year quantify the net impact of a bias in a particular variable on the simulated annual carbon balance. $\Delta_{ONland,-GEE}$ and $\Delta_{ONland,R}$ have also been introduced to indicate the smaller biases that would result from adopting a higher-resolution land cover product like the Ontario Land Cover data set, with its reported error of 10%. Here $\Delta_{\alpha\beta T_{low}},R$ is an aggregate bias resulting from assuming the incorrect relationship between T and R (Figure 7). The observed (dark green) and simulated (light green) cumulative carbon fluxes are also shown, along with the total bias (black), which is the difference between observed and simulated carbon fluxes. The sum of all biases considered in this study is shown as the dashed black line. The shaded regions for $\Delta_{LUE,-GEE}$ and $\Delta_{PAR_0},-GEE$ reflect the ranges in biases stemming from uncertainties in the fits to eddy covariance fluxes to determine "observed" PAR_0 and LUE and the negative correlations between the two parameters. See section 6.6.2 for explanation.

at annual time scales. Due to the small observed annual uptake of −0.16 t C/ha at QC, almost any source of error considered here (except for $\Delta_{T,-GEE}$) would comprise an important fraction of the annual uptake value.

[78] At ON (Figure 11) the biases due to T are likewise small, and the sunny bias in SW also resulted in an overestimate of carbon uptake of ~1 t C/ha over a year. Nonetheless the bias attributed to SW, at −1.05 t C/ha over a year, is smaller, at 26% of the total bias. $\Delta_{land,-GEE}$ and $\Delta_{land,R}$ are the biases in NEE resulting from the 25% estimated error in land cover (section 4.3). These results were derived from systematically reducing the areal coverage in the evergreen vegetation class by 25% and increasing by the same amount in the "mixed forest" class. We see that the impact of land cover is relatively small in comparison to the total bias.

6.6.2. Effects of Biases in Model Parameters

[79] The largest biases at both QC and ON derive from biospheric parameters. Due to an erroneous temperature relationship for R, VPRM systematically underestimated the carbon efflux from both QC and ON (Figure 7). The underestimation in LUE observed at both sites (Figure 6) translated into positive biases in annual carbon budgets (Figures 10 and 11). Countering the positive bias from LUE was the

bias due to PAR_0. The larger value for PAR_0 assumed by VPRM resulted in more efficient carbon uptake for a given input of PAR (Figure 5).

[80] It is worth bearing in mind, however, that the "observed" PAR_0 and LUE are negatively correlated, resulting in similar covariances in the determined biases: a bias in the lower range of $\Delta_{LUE,-GEE}$ is associated with the upper range of $\Delta_{PAR_0,-GEE}$, thereby translating into smaller absolute values of biases. Conversely, a bias in the upper range of $\Delta_{LUE,-GEE}$ is associated with the lower range of $\Delta_{PAR_0,-GEE}$, enlarging the magnitudes of each of the two bias terms.

[81] If all of the biases have been accounted for, the lines in Figures 11 and 12 indicating the sum of all considered biases (dashed black) should be identical to the total observed bias (black). Thus a comparison between the sum and the total bias reveals the remaining effect of biases not yet accounted for in this framework. This remaining bias was ~1 t C/ha at QC and ~2 t C/ha at ON.

6.7. Model Structure Misrepresentation Errors

[82] Residual errors arise from uncertainties due to model structure misrepresentation (Figure 1). Evidence of the significance in such uncertainties include the unexplained
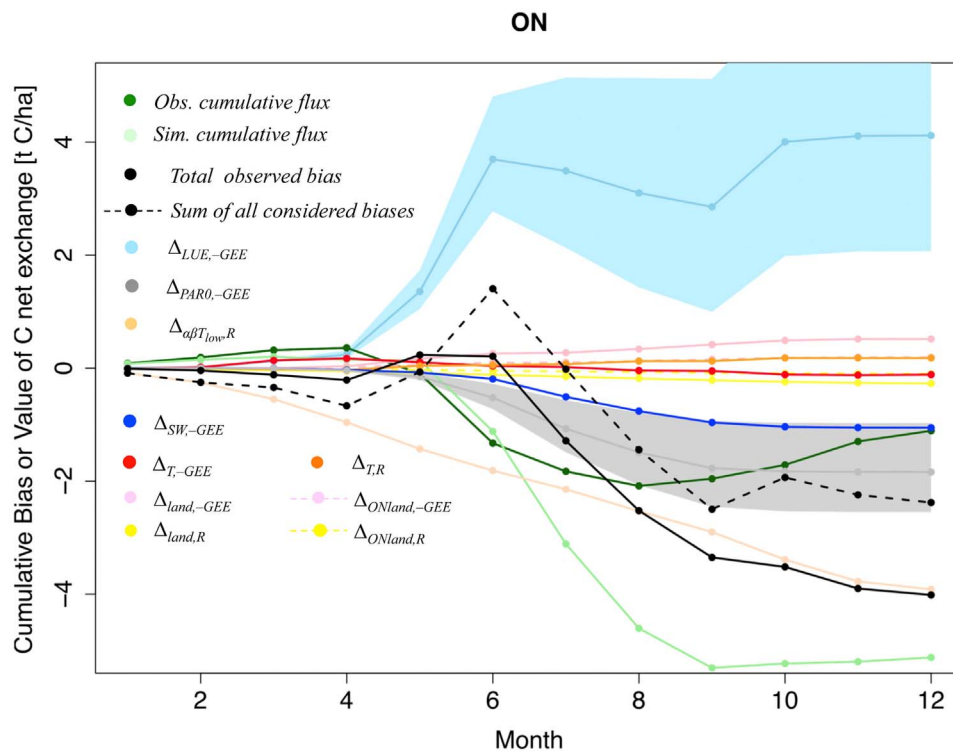
ON

Figure 11. Similar to Figure 10, for the Ontario (ON) study site.

fraction of the total variance seen in Figures 8 and 9 as well as the residual bias at annual scales of ~1 t C/ha (QC) and ~2 t C/ha (ON) seen in Figures 10 and 11.

[83] The model misrepresentation error has often been pointed out as a source of uncertainty in biospheric carbon simulations. For instance, *Amthor et al.* [2001] found model-to-model differences in annual CO_2 exchange to be larger than interannual variability in a particular model, suggesting that differences between model formulations controlled more of the changes in annual CO_2 exchange than interannual climatic variability.

[84] Errors due to model misrepresentation are more difficult to estimate than those due to model parameters. Some biospheric processes missing or misrepresented by the model can be readily identified: e.g., for VPRM, the *VPD* effect in decreasing photosynthesis [*McCaughey et al.*, 2006], as seen in ON (Figure 6b). In this case, one can explicitly quantify the error from missing processes by first incorporating the process and then comparing the result against a simulation missing the same process, as is shown in Figures 6a and 6b. Other missing processes are simply unknown, hence their absence from the model. Such errors are considered explicitly in aggregate as a residual term in the error budget, but they cannot be decomposed into contributions by specific processes.

7. Summary and Conclusions

[85] This study has introduced a framework to "unmix" contributions to the total uncertainty in simulated carbon and to attribute the total error to different factors. This error analysis framework was applied to a simple biospheric model

(VPRM) at two eddy covariance sites in central Canada, which revealed the following:

[86] 1. Random errors attributed to environmental drivers and measurement uncertainties at diurnal time scales accounted for only ≤30% of the observed variance in (obs − sim) during the peak growing months (June–August).

[87] 2. Out of all driver data sets, biases in downward shortwave radiation accumulated to the most significant amount when summed over an entire year.

[88] 3. Relatively small biases in shortwave radiation can accumulate over a year, such that they account for a significant percentage of the annually summed carbon uptake.

[89] 4. The largest biases result from PAR_0 and parameters that determine LUE and R, which can give rise to biases that are much greater than the observed annual carbon budget.

[90] 5. The total bias is the net sum of terms with large magnitudes that can differ in sign and cancel one another.

[91] It is important to point out the simplifications adopted in this paper. Errors in LUE were considered in aggregate rather than attempting to trace errors to its subcomponents: λ, T_{scale}, P_{scale}, and W_{scale}. Second, no systematic errors in eddy covariance observations were considered. While numerous authors have suggested the possibility of biased measurements, particularly during nighttime conditions [*Lee* 1998; *Sun et al.*, 1998], currently no agreement exists as to the exact size of such a bias nor ways to correct such biases.

[92] While by no means exhaustive, this study illustrates the value of a comprehensive error analysis framework. The use of the framework allows one to compare the contribution by specific variables against the total error, thereby elucidating parts of the model that need most improvements and identifying residual errors in the model.

7.1. LUE and Respiration Parameterizations

[93] The biases in PAR_0, *LUE*, and *R*, as witnessed in Figures 5–7, are symptomatic of the difficulties in spatial scaling. Such errors can accumulate to extremely large biases at seasonal to annual time scales (Figures 10 and 11) that are several times the magnitude of the annual carbon uptake. The relevant biospheric parameters for QC and ON were derived from empirical fits to eddy covariance data at the NOBS site in northern Manitoba and the Howland site in Maine, respectively [*Mahadevan et al.*, 2008], and spatially extrapolated to the two sites.

[94] Clearly, additional information is necessary to constrain seasonal to annual carbon simulations from a satellite-driven model like VPRM. Forestry-derived yield curves provide valuable constraints on annual-scale growth of trees [*Kurz et al.*, 2009]. *Matross et al.* [2006] have illustrated how atmospheric CO_2 concentrations can be used in an inverse framework to derive, at the regional scale, VPRM parameters controlling *LUE* and *R*. The temperature, phenology and water scaling factors that constrain *LUE* are difficult to estimate across landscapes. For this reason, there has been significant interest in using physiologically based reflectance indices to assess photosynthetic stress. The Photochemical Reflectance Index (PRI), for example, seems to track changes in the xanthophylls pigment status that in turn relate to light-use efficiency [*Grace et al.*, 2007; *Hilker et al.*, 2008] and this capability has been demonstrated from MODIS [*Drolet et al.*, 2008]. Nevertheless, detecting a useful PRI signal requires accounting for changes in illumination and sensor angles as well as canopy structure effects.

7.2. Implications of Biases in Model Driver Data Sets

[95] The role of driver data sets as a significant source of uncertainties in biospheric carbon modeling has been recognized only in recent few years. *Zhao et al.* [2006] and *Jung et al.* [2007] showed that the use of differing meteorological data sets is an important source of differences in the resulting biospheric carbon simulations. *Schaefer et al.* [2008] pointed out the sensitivity of biospheric model simulations to errors in environmental drivers, mentioning specifically the problems in precipitation and temperature. *Medvigy et al.* [2010] have demonstrated the importance of submonthly meteorological variability in controlling carbon uptake and noted discrepancies between variability in assimilated versus observed meteorological fields.

[96] It is important to point out that errors in environmental drivers need to be dealt with by the entire biospheric carbon modeling community, regardless of the specific model adopted. Basic drivers like temperature and solar radiation (or *PAR*) are standard input variables driving simulations of most biospheric carbon models. Errors from drivers persist even if model parameters are assigned proper values.

7.3. Relevance to Model-Data Fusion

[97] The framework described in this study and the kind of uncertainty analysis presented here constitute an important step toward a full "model-data fusion" approach. A quantitative understanding of uncertainties is critical, since the outcome of model-data fusion is determined as much by uncertainties as by the observations themselves [*Raupach*

et al., 2005]. Thus "model characterization", with an analysis of model uncertainties, is a key step within the multistage process for model-data fusion [see *Williams et al.*, 2009, Figure 1].

[98] We urge more comprehensive uncertainty analyses similar to this study to be conducted in the future and which have hitherto been lacking. To do so, model sensitivities to drivers and parameters are needed (equation (15)). While the sensitivities (partial derivatives) can be analytically derived for a simple model like the VPRM, they are not so readily obtained for more complicated biospheric models. In these cases, direct numerical simulation or a tangent linear approximation [*Giering*, 2000] is required to obtain the sensitivities. However, these sensitivities can be precalculated and placed into a look-up table to speed up the error analysis [*Leoncini et al.*, 2008].

[99] Ultimately, exercises like this study will help improve and quantify uncertainties in the land surface components of Earth system models. Because of the complexity of soil and vegetation properties, parameterization of land surface models as well as evaluating their performance over different regions are essential steps to improving confidence in global carbon balance simulations. This paper is a step toward this ultimate objective.

References

Amthor, J. S., et al. (2001), Boreal forest CO_2 exchange and evapotranspiration predicted by nine ecosystem process models: Intermodel comparisons and relations to field measurements, *J. Geophys. Res.*, *106*, 33,623–33,648, doi:10.1029/2000JD900850.

Baldocchi, D. D. (2003), Assessing the eddy covariance technique for evaluating carbon dioxide exchange rates of ecosystems: Past, present and future, *Global Change Biol.*, *9*(4), 479–492, doi:10.1046/j.1365-2486.2003.00629.x.

Barr, A. G., et al. (2004), Inter-annual variability in the leaf area index of a boreal aspen-hazelnut forest in relation to net ecosystem production, *Agric. For. Meteorol.*, *126*(3–4), 237–255, doi:10.1016/j.agrformet. 2004.06.011.

Bergeron, O., et al. (2007), Comparison of carbon dioxide fluxes over three boreal black spruce forests in Canada, *Global Change Biol.*, *13*(1), 89–107, doi:10.1111/j.1365-2486.2006.01281.x.

Betts, A., F. Chen, K. Mitchell, and Z. Janjic (1997), Assessment of the land surface and boundary layer models in two operational versions of the NCEP Eta model using FIFE data, *Mon. Weather Rev.*, *125*(11), 2896–2916, doi:10.1175/1520-0493(1997)125<2896:AOTLSA>2.0. CO;2.

Cosgrove, B. A., et al. (2003), Real-time and retrospective forcing in the North American Land Data Assimilation System (NLDAS) project, *J. Geophys. Res.*, *108*(D22), 8842, doi:10.1029/2002JD003118.

Coursolle, C., et al. (2006), Late-summer carbon fluxes from Canadian forests and peatlands along an east–west continental transect, *Can. J. For. Res.*, *36*, 783–800, doi:10.1139/x05-270.

Crutzen, P. J., and E. F. Stoermer (2000), The Anthropocene, *Global Change Newsl.*, *41*, 17–18.

Davi, H., et al. (2005), Modelling carbon and water cycles in a beech forest: Part II. Validation of the main processes from organ to stand scale, *Ecol. Modell.*, *185*, 387–405, doi:10.1016/j.ecolmodel.2005.01.003.

Davidson, E. A., I. A. Janssens, and Y. Luo (2006), On the variability of respiration in terrestrial ecosystems: Moving beyond Q_{10}, *Global Change Biol.*, *12*(2), 154–164, doi:10.1111/j.1365-2486.2005.01065.x.

Drolet, G. G., et al. (2008), Regional mapping of gross light-use efficiency using MODIS spectral indices, *Remote Sens. Environ.*, *112*, 3064–3078, doi:10.1016/j.rse.2008.03.002.

Dufresne, J.-L., et al. (2002), On the magnitude of positive feedback between future climate change and the carbon cycle, *Geophys. Res. Lett.*, *29*(10), 1405, doi:10.1029/2001GL013777.

Ehleringer, J. R., and C. B. Field (Eds.) (1993), *Scaling Physiological Processes: Leaf to Globe*, 388 pp., Academic, San Diego, Calif.

Falge, E., et al. (2001), Gap filling strategies for defensible annual sums of net ecosystem exchange, *Agric. For. Meteorol.*, *107*(1), 43–69, doi:10.1016/S0168-1923(00)00225-2.

Friedlingstein, P., et al. (2006), Climate–carbon cycle feedback analysis: Results from the C^{4}MIP model intercomparison, *J. Clim.*, *19*(14), 3337–3353, doi:10.1175/JCLI3800.1.

Giering, R. (2000), Tangent linear and adjoint biogeochemical models, in *Inverse Methods in Global Biogeochemical Cycles*, edited by P. Kasibhatla et al., pp. 33–48, AGU, Washington, D. C.

Grace, J., et al. (2007), Can we measure terrestrial photosynthesis from space directly using spectral reflectance and fluorescence, *Global Change Biol.*, *13*, 1484–1497, doi:10.1111/j.1365-2486.2007.01352.x.

Grant, R. F., et al. (2006), Net ecosystem productivity of boreal aspen forests under drought and climate change: Mathematical modelling with *Ecosys*, *Agric. For. Meteorol.*, *140*, 152–170, doi:10.1016/j.agrformet.2006.01.012.

Heinsch, F. A., et al. (2003), *User's Guide: GPP and NPP (MOD17A2/A3) Products, NASA MODIS Land Algorithm*, version 2.0, 57 pp.

Hilker, T., et al. (2008), The use of remote sensing in light use efficiency based models of gross primary production: A review of current status and future requirements, *Sci. Total Environ.*, *404*, 411–423, doi:10.1016/j.scitotenv.2007.11.007.

Hollinger, D. Y., and A. D. Richardson (2005), Uncertainty in eddy covariance measurements and its application to physiological models, *Tree Physiol.*, *25*, 873–885.

Jung, M., et al. (2007), Uncertainties of modeling gross primary productivity over Europe: A systematic study on the effects of using different drivers and terrestrial biosphere models, *Global Biogeochem. Cycles*, *21*, GB4021, doi:10.1029/2006GB002915.

Keeling, C. D., and T. P. Whorf (1994), Atmospheric CO_2 records from sites in the SIO air sampling network, in *Trends '93: A Compendium of Data on Global Change, Oak Ridge Natl. Lab. Rep., ORNL, CDIAC-65*, pp. 16–26, Oak Ridge Natl. Lab., Oak Ridge, Tenn.

Kicklighter, D. W., A. Bondeau, A. L. Schloss, J. Kaduk, A. D. McGuire, and the participants of the Potsdam NPP model intercomparison (1999), Comparing global models of terrestrial net primary productivity (NPP): Global pattern and differentiation by major biomes, *Global Change Biol.*, *5*, suppl. 1, 16–24, doi:10.1046/j.1365-2486.1999.00003.x.

Kucharik, C. J., et al. (2006), A multiyear evaluation of a Dynamic Global Vegetation Model at three AmeriFlux forest sites: Vegetation structure, phenology, soil temperature, and CO_2 and H_2O vapor exchange, *Ecol. Modell.*, *196*(1–2), 1–31, doi:10.1016/j.ecolmodel.2005.11.031.

Kurz, W., and M. J. Apps (1999), A 70-year retrospective analysis of carbon fluxes in the Canadian forest sector, *Ecol. Appl.*, *9*(2), 526–547, doi:10.1890/1051-0761(1999)009[0526:AYRAOC]2.0.CO;2.

Kurz, W. A., et al. (2009), CBM-CFS3: A model of carbon-dynamics in forestry and land-use change implementing IPCC standards, *Ecol. Modell.*, *220*(4), 480–504, doi:10.1016/j.ecolmodel.2008.10.018.

Lee, X. (1998), On micrometeorological observations of surface–air exchange over tall vegetation, *Agric. For. Meteorol.*, *91*(1–2), 39–49, doi:10.1016/S0168-1923(98)00071-9.

Leoncini, G., R. A. Pielke Sr., and P. Gabriel (2008), From model-based parameterizations to lookup tables: An EOF approach, *Weather Forecast.*, *23*(6), 1127–1145, doi:10.1175/2008WAF2007033.1.

Loveland, T. R., et al. (2000), Development of a global land cover characteristics database and IGBP DISCover from 1-km AVHRR Data, *Int. J. Remote Sens.*, *21*(6–7), 1303–1330, doi:10.1080/014311600210191.

Mahadevan, P., et al. (2008), A satellite-based biosphere parameterization for net ecosystem CO_2 exchange: Vegetation Photosynthesis and Respiration Model (VPRM), *Global Biogeochem. Cycles*, *22*, GB2005, doi:10.1029/2006GB002735.

Margolis, H. A., L. B. Flanagan, and B. D. Amiro (2006), The Fluxnet-Canada Research Network: Influence of climate and disturbance on carbon cycling in forests and peatlands, *Agric. For. Meteorol.*, *140*, 1–5, doi:10.1016/j.agrformet.2006.08.013.

Matross, D. M., et al. (2006), Estimating regional carbon exchange in New England and Québec by combining atmospheric, ground-based and satellite data, *Tellus, Ser. B*, *58*, 344–358, doi:10.1111/j.1600-0889.2006.00206.x.

McCaughey, J. H., M. R. Pejam, M. A. Arain, and D. A. Cameron (2006), Carbon dioxide and energy fluxes from a boreal mixedwood forest ecosystem in Ontario, Canada, *Agric. For. Meteorol.*, *140*, 79–96, doi:10.1016/j.agrformet.2006.08.010.

Medvigy, D., S. C. Wofsy, J. W. Munger, and P. R. Moorcroft (2010), Responses of terrestrial ecosystems and carbon budgets to current and future environmental variability, *Proc. Natl. Acad. Sci. U. S. A.*, *107*(18), 8275–8280, doi:10.1073/pnas.0912032107.

Mitchell, K. E., et al. (2004), The multi-institution North American Land Data Assimilation System (NLDAS): Utilizing multiple GCIP products and partners in a continental distributed hydrological modeling system, *J. Geophys. Res.*, *109*, D07S90, doi:10.1029/2003JD003823.

Nobel, P. S. (1999), *Physiochemical and Environmental Plant Physiology*, 2nd ed., Academic, San Diego, Calif.

Ontario Ministry of Natural Resources (2002), Ontario provincial-scale land cover, Ont. Min. of Nat. Res., Peterborough, Ont., Canada.

Pejam, M. R., M. A. Arain, and J. H. McCaughey (2006), Energy and water vapour exchanges over a mixedwood foreal forest in Ontario, Canada, *Hydrol. Process.*, *20*, 3709–3724, doi:10.1002/hyp.6384.

Raupach, M. R., et al. (2005), Model-data synthesis in terrestrial carbon observation: Methods, data requirements and data uncertainty specifications, *Global Change Biol.*, *11*(3), 378–397, doi:10.1111/j.1365-2486.2005.00917.x.

Rodgers, C. D. (2000), *Inverse Methods for Atmospheric Sounding: Theory and Practice*, World Sci., Hackensack, N. J.

Sacks, W. J., D. S. Schimel, R. K. Monson, and B. H. Braswell (2006), Model-data synthesis of diurnal and seasonal CO_2 fluxes at Niwot Ridge, Colorado, *Global Change Biol.*, *12*, 240–259, doi:10.1111/j.1365-2486.2005.01059.x.

Schaefer, K., et al. (2008), Combined simple biosphere/Carnegie-Ames-Stanford approach terrestrial carbon cycle model, *J. Geophys. Res.*, *113*, G03034, doi:10.1029/2007JG000603.

Schulze, E., et al. (1994), Relationships among stomatal conductance, ecosystem surface conductance, carbon assimilation rate, and plant nitrogen nutrition: A global scaling exercise, *Annu. Rev. Ecol. Syst.*, *25*, 629–662, doi:10.1146/annurev.es.25.110194.003213.

Sun, J., R. Desjardins, L. Mahrt, and I. MacPherson (1998), Transport of carbon dioxide, water vapor, and ozone by turbulence and local circulations, *J. Geophys. Res.*, *103*(D20), 25,873–25,885, doi:10.1029/98JD02439.

Sun, J., et al. (2008), Simulating carbon exchange of Canadian boreal forests: II. Comparing the carbon budgets of a boreal mixedwood stand to a black spruce forest stand, *Ecol. Modell.*, *219*(3–4), 276–286, doi:10.1016/j.ecolmodel.2008.03.031.

Taylor, J. R. (1997), *An Introduction to Error Analysis: The Study of Uncertainty in Physical Measurements*, 2nd ed., Univ. Sci. Books, Sausalito, Calif.

Vermote, E. F., and S. Kotchenova (2008), Atmospheric correction for the monitoring of land surfaces, *J. Geophys. Res.*, *113*, D23S90, doi:10.1029/2007JD009662.

Vermote, E. F., and N. Saleous (2006), Operational atmospheric correction of MODIS visible to middle infrared land surface data in the case of an infinite Lambertian target, in *Earth Science Satellite Remote Sensing: Science and Instruments*, vol. 1, edited by J. J. Qu et al., pp. 123–153, Springer, New York, doi:10.1007/978-3-540-37293-6_8

Vermote, E. F. and A. Vermeulen (1999), Atmospheric correction algorithm: Spectral reflectances (MOD09), MODIS ATBD Ver. 4.0, NASA Contract NAS5-96062, NASA, Washington, D. C.

Williams, M., Y. Malhi, A. D. Nobre, E. B. Rastetter, J. Grace, and M. G. P. Pereira (1998), Seasonal variation in net carbon exchange and evapotranspiration in a Brazilian rain forest: A modeling study, *Plant Cell Environ.*, *21*(10), 953–968, doi:10.1046/j.1365-3040.1998.00339.x.

Williams, M., et al. (2009), Improving land surface models with FLUXNET data, *Biogeosciences*, *6*(7), 1341–1359, doi:10.5194/bg-6-1341-2009.

Xiao, X., et al. (2004), Satellite-based modeling of gross primary production in an evergreen needleleaf forest, *Remote Sens. Environ.*, *89*(4), 519–534, doi:10.1016/j.rse.2003.11.008.

Zhao, M., et al. (2006), Sensitivity of Moderate Resolution Imaging Spectroradiometer (MODIS) terrestrial primary production to the accuracy of meteorological reanalyses, *J. Geophys. Res.*, *111*, G01002, doi:10.1029/2004JG000004.

Zhou, X., et al. (2008), Simulating carbon exchange in Canadian Boreal forests: I. Model structure, validation, and sensitivity analysis, *Ecol. Modell.*, *219*(3–4), 287–299, doi:10.1016/j.ecolmodel.2008.07.011.

———————
E. Chan and J. C. Lin, Department of Earth and Environmental Sciences, University of Waterloo, 200 University Ave. W., Waterloo, ON N2L 3G1, Canada.

E. W. Gottlieb and S. C. Wofsy, Department of Earth and Planetary Science, Harvard University, 20 Oxford St., Cambridge, MA 02138, USA.

H. A. Margolis, Centre d'Études de la Forêt, Faculté de Foresterie, de Géographie et de Géomatique, Université Laval, Québec, QC G1V 0A6, Canada.

J. H. McCaughey, Department of Geography, Queen's University, Mackintosh-Corry Hall, Rm. D201, Kingston, ON K7L 3N6, Canada.

M. R. Pejam, Climate Research Division, Environment Canada, 4905 Dufferin St., Toronto, ON M3H 5T4, Canada.